Ice-flow characteristics over a rough bedrock: implications for ice-core interpretation

Frank PATTYN

Department of Geography
Vrije Universiteit Brussel
Pleinlaan 2, B-1050 Brussel, Belgium

POLAR METEOROLOGY AND GLACIOLOGY 16: 42–52

Abstract

Recent observations in western Dronning Maud Land, Antarctica, point to a relatively high bedrock roughness in the area of the future EPICA drilling site. It is commonly accepted that such a roughness does not favor the interpretation of deep ice cores as basal ice-sheet interactions might disturb the bottom ice layers. The present study aims at examining the ice-flow characteristics over a strongly undulating bed and investigates its influence on age-depth profiles in the ice sheet.

For this purpose a high-resolution time-dependent two-dimensional flowline model was developed (horizontal gridsize $\leq$1 km), taking into account all relevant stresses at such a small scale. The model is solved on a fixed finite-difference grid, and compared with a similar model, solving the velocity field according to the *shallow-ice approximation*. The analysis is presented for sinusoidal bedrock undulations with amplitude-to-wavelength ratio comparable to those observed by radio-echo sounding (STEINHAGE *et al.*, 1999). Calculations are performed over a period of 300 ka. Results demonstrate that the influence of a high bed roughness on the age-depth profiles is not only confined close to the bed, but near the surface as well, which might affect the interpretation of shallow ice cores.

Introduction

Recent observations – based on aerial radio-echo sounding – in the vicinity of the future EPICA[1] ice-core drilling site in Dronning Maud Land, Antarctica, show that the subglacial topography is highly accidented (STEINHAGE *et al.*, 1999). Moreover, the selected drilling site is – contrary to the Dome Fuji drilling site – not situated on a divide. Both factors contribute to the complexity of the ice flow in the vicinity of the future drilling site, which might hamper the interpretation of the ice core in terms of particle origin and ice age. There is no doubt that complex numerical models will become necessary for the dating as well as the interpretation of the ice core. Some preliminary studies along these lines have already been carried out (e.g. SAVVIN *et al.*, 2000), using grid sizes of 10 km and beyond, and thus overseeing smaller-scale roughness.

This study focuses on the characteristics of the ice flow over a strongly undulating bedrock in slow-moving areas of the ice sheet (near divide conditions). We therefore considered bedrock perturbations of the order of magnitude as those observed in Dronning Maud Land (STEINHAGE *et al.*, 1999). The analysis is based on a high-resolution time-dependent two-dimensional flowline model with a horizontal gridsize of $\leq$1 km, taking into account all relevant stresses at such a small scale (PATTYN, 2000). The model is solved on a fixed finite-difference grid and compared with a similar model, solving the velocity field according to the shallow-ice approximation.

The ice-sheet model

Field equations

The developed numerical ice sheet model is a dynamic flowline model that predicts the ice thickness distribution along a fixed flowline in space in response to environmental conditions (PATTYN, 2000). This response is obtained by calculating at a given moment the two-dimensional flow regime, determined by the ice sheet geometry and its boundary conditions. A detailed description of the ice-sheet model is given in PATTYN (2002). Only a brief overview of the major components of the model will be presented here.

A Cartesian coordinate system (x, z) with the x-axis along the flowline, parallel to the geoid and the z-axis vertically pointing upward (z = 0 at sea level) is defined. This implies that the only non-zero velocity components are u, w (horizontal and vertical velocity, respectively), while the horizontal transverse velocity v = 0. Convergence and divergence of the ice flow leads to $\frac{\partial v}{\partial y} = \frac{u}{\omega}\frac{\partial \omega}{\partial x}$, where ω is the width along the flowline. Mass conservation and the stress equilibrium thus become

$$\frac{\partial u}{\partial x} + \frac{u}{\omega}\frac{\partial \omega}{\partial x} + \frac{\partial w}{\partial z} = 0\,, \tag{1}$$

$$\frac{\partial \sigma_{xx}}{\partial x} + \frac{\partial \sigma_{xz}}{\partial z} = 0\,,$$

$$\frac{\partial \sigma_{xz}}{\partial x} + \frac{\partial \sigma_{zz}}{\partial z} = \rho g\,, \tag{2}$$

where ρ is the ice density (910 kg m^{-3}), g the gravitational acceleration (9.81 m s^{-2}), and $[\sigma]$ the stress tensor. For an isotropic ice mass that deforms under steady state creep, the constitutive equation, relating the deviatoric stresses to the strain-rates is expressed as (PATERSON, 1994)

[1] EPICA: European Project on Ice Coring in Antarctica

$$\sigma'_{ij} = 2\eta\dot{\varepsilon}_{ij}, \quad \eta = \frac{1}{2}A^{-\frac{1}{n}}\left(\dot{\varepsilon}+\dot{\varepsilon}_0\right)^{\frac{1-n}{n}} , \tag{3}$$

for $i, j = x, y, z$, where $\dot{\varepsilon}$ is the second strain-rate tensor invariant defined by $\dot{\varepsilon}^2 = \sum_{ij}\frac{1}{2}\dot{\varepsilon}_{ij}\dot{\varepsilon}_{ij}$ and η is the effective viscosity. $\dot{\varepsilon}_0$ is a small number (10^{-30}) to validate Glen's flow law in cases where $\dot{\varepsilon}$ equals zero, and singularity might occur. The use of such a small number does not influence the numerical outcome of the model. A is the flow-law parameter and $n = 3$ is the power law exponent of Glen's flow law. Deviatoric stresses are related to the stress components by $\sigma'_{ii} = \sigma_{ii} - \frac{1}{3}(\sigma_{xx}+\sigma_{yy}+\sigma_{zz})$ and $\sigma'_{ij} = \sigma_{ij}$, for $i \neq j$, so that the stress equilibrium (Equation 2) can be written as

$$2\frac{\partial\sigma'_{xx}}{\partial x} + \frac{\partial\sigma'_{yy}}{\partial x} + \frac{\partial^2}{\partial x^2}\int_z^s \sigma'_{xz}\,dz + \frac{\partial\sigma'_{xz}}{\partial z} = \rho g\frac{\partial(s-z)}{\partial x} , \tag{4}$$

where s is the surface of the ice mass. The third term of the left-hand side of Equation 4 can be written as $\frac{\partial R_{zz}}{\partial x}$, where R_{zz} represents the vertical resistive stress (VAN DER VEEN and WHILLANS, 1989). Starting from the known bedrock topography and surface mass balance distribution, and assuming a constant ice density, the change of ice thickness along the flow line is predicted as

$$\frac{\partial H}{\partial t} = -\frac{1}{\omega}\frac{\partial(\overline{u}H\omega)}{\partial x} + M_s , \tag{5}$$

where $\overline{u}$ is the depth averaged horizontal velocity (m a^{-1}), H the ice thickness (m), and M_s the surface mass balance (m a^{-1} ice equivalent). Boundary conditions to the ice sheet are a symmetric ice divide ($\frac{\partial s}{\partial x} = \frac{\partial H}{\partial x} = 0$); zero ice thickness at the seaward side; a stress-free surface, a kinematic boundary condition to the vertical velocity based on mass conservation, and no-sliding conditions at the bottom of the ice sheet.

Age calculation

The age calculation within the ice sheet is written as an advection equation with a small diffusion term added in order to stabilize the numerical solution (HUYBRECHTS, 1994; GREVE, 1997)

$$\frac{\partial\mathcal{A}}{\partial t} = 1 - u\frac{\partial\mathcal{A}}{\partial x} - w\frac{\partial\mathcal{A}}{\partial z} + D_{\text{art}}\frac{\partial^2\mathcal{A}}{\partial z^2} \tag{6}$$

where $\mathcal{A}$ is the ice age (a), and D_{art} a constant diffusion term (5.0 10^{-8} m^2 a^{-1}; MÜGGE *et al.*, 1999). Boundary conditions to this equation are $\mathcal{A}(s) = 0$ at the surface and a constant thinning factor at the bottom of the ice mass of $m_{\text{age}} = 200$. For a mean surface accumulation of $M_{\text{mean}} = 0.3$ m a^{-1}, the basal boundary condition is written as $\frac{\partial\mathcal{A}}{\partial z}(b) = -m_{\text{age}}/M_{\text{mean}}$ (GREVE, 1997). Experiments with different values for this thinning factor showed that only the lower 10% of the ice sheet is slightly influenced by the choice in m_{age}.

Numerical solution

For numerical convenience a dimensionless vertical coordinate is introduced to account for ice-thickness variations along the flowline, which is defined as $\zeta = (s-z)/H$, so that $\zeta = 0$ at the upper surface and $\zeta = 1$ at the base of the ice sheet. After this transformation, all equations are solved on an irregular spaced grid in both x and ζ. The vertical domain is subdivided in 30 layers with varying thickness, i.e. a lowermost grid spacing of 0.015, gradually increasing towards the top of the ice column (Figure 1). Central differences are

used to compute first- and second-order gradients. At the boundaries, upstream and downstream differences are employed (e.g. PAYNE and DONGELMANS, 1997).

An expression for the velocity field is found by relating the strain-rates to velocity gradients ($\dot{\varepsilon}_{ij} = \frac{1}{2}\left(\frac{\partial u_i}{\partial x_j} + \frac{\partial u_j}{\partial x_i}\right)$) and inserting Equation 3 into Equation 4. After introducing the dimensionless vertical co-ordinate, the finite difference form of this equation is written as a set of linear equations with $u(x,\zeta)$ as unknowns. This set is solved by the conjugate gradient method on sparse matrices (PRESS *et al.*, 1992). However, due to the non-linear nature of the flow-law (Equation 3) and the dependence of η on $\dot{\varepsilon}$ and hence on u, a proper solution to the velocity field is found in an iterative fashion using a Picard iteration. In order to optimize the convergence a relaxation formula was added using the subspace iteration scheme described by HINDMARSH and PAYNE (1996). The age equation (Equation 6) is solved using a three-point dissymmetric upwind differencing scheme.

Shallow-ice approximation

For the purpose of this paper, experiments carried out with the higher-order model (HO) were compared to a similar model that solves the velocity field according to the 'shallow-ice approximation' (SI). The horizontal velocity in the grounded ice sheet according to SI is determined as (e.g. HUYBRECHTS and OERLEMANS, 1988)

$$u(z) - u_b = -2A(\rho g)^n \left|\frac{\partial s}{\partial x}\right|^{n-1} \frac{\partial s}{\partial x} \int_h^z (s-z)^n \, dz \,. \tag{7}$$

Numerical experiments

Model setup

For all experiments we considered an ice sheet resting on a flat bedrock. A sine-wave bedrock perturbation was then introduced, situated at a distance of 30 km from the ice divide. The sine-wave perturbation is defined as a two-term harmonic wave in order to guarantee a smooth transition between the perturbed and unperturbed area

$$h_b = A_m \sin\left(\frac{2\pi x}{\lambda}\right) - \frac{1}{2} A_m \sin\left(\frac{4\pi x}{\lambda}\right) \tag{8}$$

where the amplitude of the bed perturbation is taken as A_m = 500 m, and the wavelength defined as λ = 20 km. Surface mass balance was taken constant over the whole length of the flowline, i.e. M_s = 0.3 m a^{-1}. An irregular gridsize was employed, allowing for grid spacings of 1 km in the vicinity of the bedrock perturbation. The model calculations were performed over a time span of 300 ka. Two types of experiments were carried out, i.e. *fixed-geometry* and *steady-state* experiments. For the *fixed-geometry* experiments a uniform slab of ice of H = 1 500 m was considered with a gentle slope of α = 0.002. For the *steady-state* experiments, the model ice sheet was allowed to react to the environmental conditions and was run forward in time until a steady state condition was achieved. The flow-law parameter was set to $A = 10^{-17}$ Pa^{-n} a^{-1}. The steady-state profile and the numerical grid are shown in Figure 1.

Fixed-geometry experiments (FGE)

Figure 2 displays the horizontal velocity field for the *fixed-geometry* experiments according to both numerical models. This figure clearly demonstrates the effect of higher-order stresses, primarily the longitudinal stress gradients. According to SI (Equation 7), the horizontal velocity is locally determined and hence only a function of the local ice geometry. Since in this experiment the surface slope is kept constant, but the ice thickness varies over the bedrock perturbations, the velocity field is a function of these local ice thickness variations. The highest velocity is thus encountered in areas where the ice is thick, i.e. in the troughs, while the smallest velocity is observed over the bumps.

According to HO, the velocity field is smoothed out over the whole model domain (Figure 2). The maximum velocity is still encountered in the troughs, but longitudinal pushes and pulls – due to the bedrock perturbation – influence the velocity field in a global way and not locally as is the case with SI. Such smoothing of velocity and stress fields is typical for higher-order models (e.g. BLATTER *et al.*, 1998).

Thicker ice (H = 2 000–2 500 m) changes the absolute values of the velocity field in both experiments (increase in ice velocity), but does not influence the pattern in the velocity and stress field for both SI and HO.

Steady-state experiments (SSE)

As seen from Figure 3, the differences in velocity field between both models – as encountered in FGE – disappear for SSE. Both velocity fields (HO and SI) are virtually the same. However, the physics that describe both models are different, and, as shown by FGE, must give rise to a more pronounced differentiation between both models. This differentiation is not displayed in the velocity or stress fields calculated according to both models, but in the ice-sheet geometry (Figure 4). The ice-sheet geometry was allowed to adjust to the stress-field conditions, which results in (i) a lower surface profile according to HO of 5 to 10 m compared to SI – this difference increases as the velocity increases – and (ii) more pronounced surface gradients according to HO. These geometrical differences between both model results are only pronounced in the vicinity of the bedrock perturbations. Outside this zone these differences disappear, which confirms the viability of the *shallow-ice approximation* for large ice masses characterized by small surface and bedrock slopes.

Another marked difference between SSE and FGE is that the maximum of the horizontal velocity is not reached in the troughs, i.e. where the ice is thick, but on top of the bumps, where the ice is shallow. The highest velocities are now associated with the maximum surface gradients. Hence, the dominant factor controlling the velocity field now becomes the surface slope instead of the ice thickness.

The age distribution within the ice sheet and the associated annual layer thickness are displayed in Figure 5. The age profile $\mathcal{A}(z)$ along a vertical line through the ice sheet and the vertically measured annual layer-thickness profile $\lambda(z)$ are related by (REEH, 1989)

$$\mathcal{A}(z) = \int_{z}^{s} \frac{\mathrm{d}z}{\lambda(z)} \tag{9}$$

Isochronous layers are parallel to the bedrock perturbations and become smoothed out towards the surface of the ice sheet. There is no discontinuity within the isochronous layering, since there is no flow deviation from the plane parallel to flow 'around' the bump.[2] All ice is supposed to flow uniformly over the

[2] A bump of infinite length in the y-direction is considered.

bump. The annual layer thickness displays a similar pattern of isochronous layers parallel to the bedrock undulations. However, the distortion is not smoothed out in the vertical, and close to the surface of the ice mass the annual layer thickness remains highly disturbed (Figure 5). This distortion implies a thickening of the annual layers close to the surface above the bedrock trough. The annual layer thickness in this distorted zone is larger than the surface accumulation rate and hence must be due to differences in ice dynamics close to the surface. For instance, at a depth of 300 m below the surface, the annual layer thickness is twice as large over a trough than over bump (Figure 6), even though surface accumulation is the same at both sites. This difference is due to an increase in annual layer thickness with depth in the top 200 m of the ice sheet over a trough, while outside these zones, annual layer thickness gradually decreases with depth.

Discussion

Flank-flow index

To investigate the ice-dynamical properties of the flow over the bedrock bumps we defined the depth-dependent flank-flow index (MARSHALL and CUFFEY, 2000)

$$f(z) = \frac{S(z)}{S(z)+P(z)} \tag{10}$$

$$S(z) = |\dot{\varepsilon}_{xz}| \approx \frac{1}{2}\left|\frac{\partial u}{\partial z}+\frac{\partial w}{\partial x}\right| \tag{11}$$

$$P(z) = |\dot{\varepsilon}_{xx}+\dot{\varepsilon}_{yy}| \approx \left|\frac{\partial u}{\partial x}+\frac{u}{\omega}\frac{\partial \omega}{\partial x}\right| \tag{12}$$

where $S(z)$ and $P(z)$ indicate the strain rates associated with simple shear and pure shear at elevation z in the ice mass, respectively. A divide-flow regime is characterized by negligible simple shear stress (S = 0), while simple shear dominates pure strain in the flank-flow regime (RAYMOND, 1983; MARSHALL and CUFFEY, 2000). The flank-flow index for the numerical experiment is displayed in Figure 7: (i) high values for f correspond to areas dominated by shear strain and are found close to the bed. The highest values are situated over the flat bedrock areas and right on the bumps and in the troughs of the bedrock perturbations. Near the high bedrock slopes a mixed regime is observed where both simple shear and pure strain exist. (ii) Near the surface, pure strain is dominant (low values of f), although higher values of f occur in the zone corresponding to the bedrock bumps. The distortion in annual layer thickness apparently coincides with zones where the ice flow changes from this simple shear regime close to the surface to pure shear, or where the longitudinal stress gradient increases due to increased stretching of the ice layers in the horizontal. This stretches out the ice layers instead of compressing them so that a local thickening in the annual layers can be observed (Figure 5 and 6).

Are distortions numerical artifacts?

Numerical finite difference schemes are known to be conditionally unstable for pure advection equations, such as the age equation (Equation 6). A common method to stabilize the solution of these equations is by using an upstream differencing scheme and adding a small amount of artificial diffusion along the vertical. Horizontal gradients are commonly determined using a dissymmetric upwind differencing scheme involving three gridpoints (e.g. HUYBRECHTS, 1994). However, in a Lagrangian coordinate system, the age equation is by definition reduced to

$$\frac{\mathrm{d}\mathcal{A}}{\mathrm{d}t} = 1 \tag{13}$$

with the boundary condition $\mathcal{A}(z = s) = 0$. The solution to Equation 13 is very simple: each year an ice particle becomes one year older. We thus need to determine the position of the particle in time using a particle-tracing algorithm, i.e.

$$\frac{\mathrm{d}\vec{\mathbf{x}}}{\mathrm{d}t} = \vec{\mathbf{u}}(x, z, t) \tag{14}$$

Equation 14 is numerically integrated using a 4^{th}-order Runge-Kutta scheme. Such forward integration enables us to determine the particle paths in the ice sheet and – after interpolation – the age and annual layer thickness. The advantage of this method is that numerical artifacts due to artificial diffusion processes are eliminated. A drawback, however, is that the numerical integration is time-consuming and that the result must be interpolated onto the numerical grid. Results of the particle-tracing algorithm applied to the ice flow over the bedrock perturbations confirmed the existence of the distortion in annual layer thickness near the surface, which indicates that this cannot be considered as an numerical artifact.

Implications for ice-core interpretation

OERTER *et al.* (2000) compiled an accumulation map of western Dronning Maud Land based on recently obtained shallow firn cores. This map shows a rather large spatial variability of accumulation rate, ranging from 40 to 90 kg m^{-2} a^{-1}. Such high variability in surface accumulation rates in western Dronning Maud Land was already observed by MELVOLD *et al.* (1998) along a traverse extending from the coast to polar plateau. The authors addressed this large variability on both mesoscale and microscale due to complex patterns of precipitation controlled by orography and redistribution by katabatic winds. It is not excluded that annual layer thickness – as interpreted from shallow firn and ice cores – is influenced by the strong bedrock irregularities as demonstrated by the numerical experiments. However, it will be very difficult to distinguish this effect from other influences – such as redistribution of snow due to katabatic wind activity – on the local and regional accumulation patterns of the Antarctic ice sheet.

Conclusions

Using a high-resolution higher-order numerical ice-sheet model, we investigated the ice flow in the interior of the ice sheet over a strongly undulating bedrock. Similar bedrock perturbations are observed in the area of the future EPICA Dronning Maud Land ice-core drilling site (STEINHAGE *et al.*, 1999). The model experiments indicate that a higher-order numerical model is necessary to simulate the ice flow over such perturbations as longitudinal stress gradients cannot be neglected and the *shallow-ice approximation* fails. These higher-order stresses influence locally and regionally the stress field within the ice mass as well as the ice-sheet geometry.

The model also demonstrated that bedrock perturbations not only influence the ice flow close to the bedrock, but also near the surface, due to the change of the ice flow from a simple shear to a pure shear flow regime. Such disturbances might affect the interpretation of shallow ice cores as well.

Acknowledgements

This paper forms a contribution to the Belgian Research programme on the Antarctic (Federal Office for Scientific, Technical and Cultural Affairs), contract EV/03/08A. This work is also a contribution to the 'European Project for Ice Coring in Antarctica (EPICA)', a joint European Science Foundation/European Commission (EC) scientific programme, funded by the EC under the Environment and Climate Programme and by national contributions from Belgium, Denmark, France, Germany, Italy, The Netherlands, Norway, Sweden, Switzerland and the United Kingdom. This is EPICA publication No.xx.

References

BLATTER, H., CLARKE, G.K.C., and COLINGE, J. (1998). Stress and velocity fields in glaciers: Part II. sliding and basal stress distribution. J. Glaciol., 44(148):457–466.

GREVE, R. (1997). Large-scale ice-sheet modelling as a means of dating deep ice cores in Greenland. J. Glaciol., 43(144):307–310.

HINDMARSH, R.C.A. and PAYNE, A.J. (1996). Time-step limits for stable solutions of the ice-sheet equation. Ann. Glaciol., 23:74–85.

HUYBRECHTS, P. (1994). The present evolution of the Greenland ice sheet: An assessment by modelling. Global and Planetary Change, 9:39–51.

HUYBRECHTS, P. and OERLEMANS, J. (1988). Evolution of the East Antarctic ice sheet: a numerical study of thermo-mechanical response patterns with changing climate. Ann. Glaciol., 11:52–59.

MARSHALL, S.J. and CUFFEY, K.M. (2000). Peregrinations of the Greenland Ice Sheet divide in the last glacial cycle: Implications for central Greenland ice cores. Earth and Planetary Science Letters, 179:73–90.

MELVOLD, K., HAGEN, J.O., PINGLOT, J.F., and GUNDESTRUP, N. (1998). Large spatial variation in accumulation rate in Jutulstraumen ice stream, Dronning Maud Land, Antarctica. Ann. Glaciol., 27:231–238.

MÜGGE, B., SAVVIN, A.A., CALOV, R., and GREVE, R. (1999). Numerical age computation of the Antarctic ice sheet for dating deep ice cores. In K. Hutter, Y. Wang and Beer, H., editors, Advances in Cold-Region Thermal Engineering and Sciences, pages 307–318. Springer.

OERTER, H., WILHELMS, F., JUNG-ROTHENHÄUSLER, F., GÖKTAS, F., MILLER, H., GRAF, W., and SOMMER, S. (2000). Accumulation rates in Dronning Maud Land, Antarctica, as revealed by dielectric-profiling measurements of shallow firn cores. Ann. Glaciol., 30:27–34.

PATERSON, W.S.B. (1994). The Physics of Glaciers. Oxford, Pergamon Press, 3rd edition.

PATTYN, F. (2000). Ice-sheet modelling at different spatial resolutions: Focus on the grounding line. Ann. Glaciol., 31:211–216.

PATTYN, F. The response of glaciers and ice sheets to climate change using a higher-order numerical ice-flow model. submitted to J. Glaciol., 2002.

PAYNE, A.J. and DONGELMANS, P.W. (1997). Self-organisation in the thermomechanical flow of ice sheets. J. Geophys. Res., 102(B6):12219–12234.

PRESS, W.H., TEUKOLSKY, S.A., VETTERLING, W.T., and FLANNERY, B.P. (1992). Numerical Recipes in C: The Art of Scientific Computing. Cambridge University Press (Cambridge), 2nd edition.

RAYMOND, C.F. (1983). Deformation in the vicinity of ice divides. J. Glaciol., 29:357–373.

REEH, N. (1989). Dating by ice flow modeling: A useful tool or an excercise in applied mathematics? In Oescher, H. and Langway, C.C., editors, The Environmental Record in Glaciers and Ice Sheets, pages 141–159. John Wiley and Sons.

SAVVIN, A., GREVE, R., CALOV, R., MÜGGE, B., and HUTTER, K. (2000). Simulation of the Antarctic ice sheet with a three- dimensional polythermal ice-sheet model, in support of the EPICA project. II. Nested high-resolution treatment of Dronning Maud Land. Ann. Glaciol., 30:69–75.

STEINHAGE, D., NIXDORF, U., MEYER, U., and MILLER, H. (1999). New maps of the ice thickness and subglacial topography in Dronning Maud Land, Antarctica, determined by means of airborne radio-echo sounding. Ann. Glaciol., 29:267–272.

VAN DER VEEN, C.J. and WHILLANS, I.M. (1989). Force budget: I. theory and numerical methods. J. Glaciol., 35(119):53–60.

List of Figures

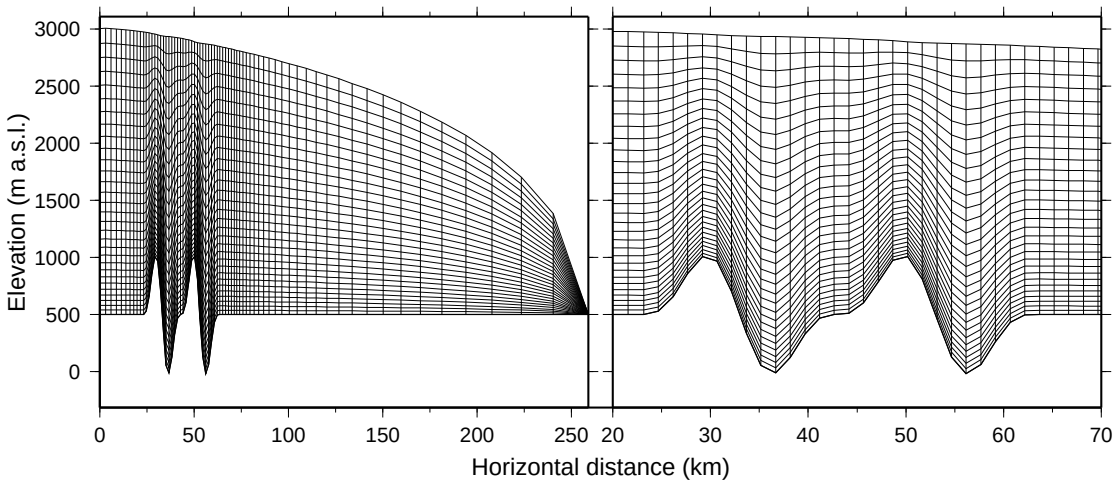

Figure 1: *Ice-sheet geometry for the steady-state experiment. The left panel shows the whole numerical model domain characterized by an irregular grid spacing in both horizontal and vertical direction. The right panel shows a detail of the domain in the vicinity of the bedrock irregularities. Ice flow is from left to right.*

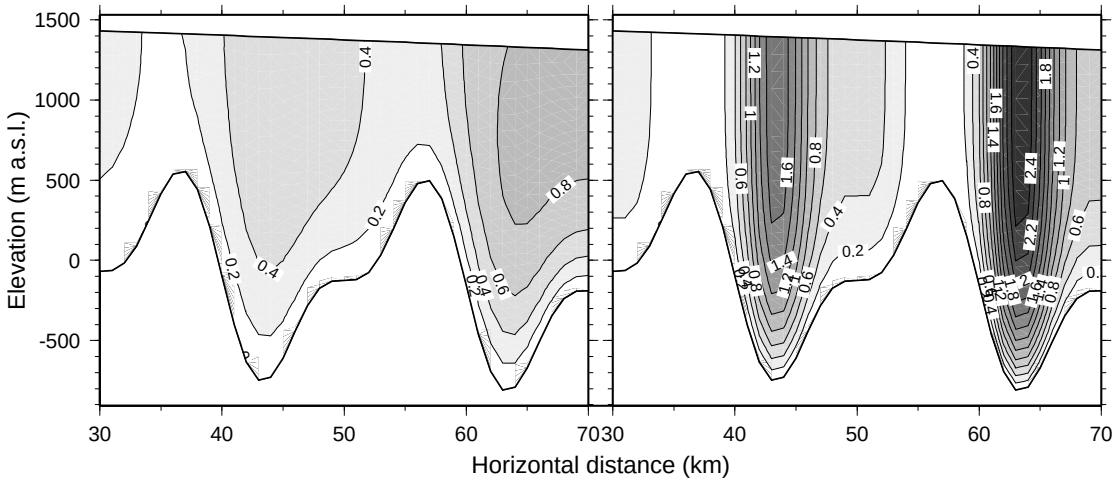

Figure 2: *Along-flow (horizontal) velocity distribution in the ice sheet for the fixed-geometry experiment. Left panel shows the result (m* a^{-1}*) for* HO*, while the right panel shows the velocity field according to* SI*. Ice flow is from left to right.*

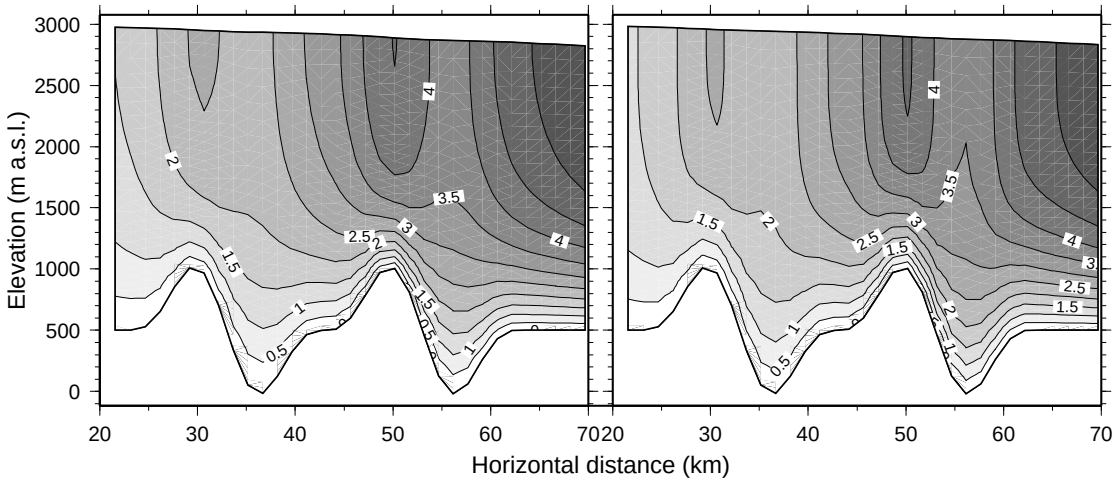

Figure 3: *Along-flow (horizontal) velocity distribution in the ice sheet for the steady-state experiment. Left panel shows the result (m* a^{-1}*) for* HO*, while the right panel shows the velocity field according to* SI*. Ice flow is from left to right.*

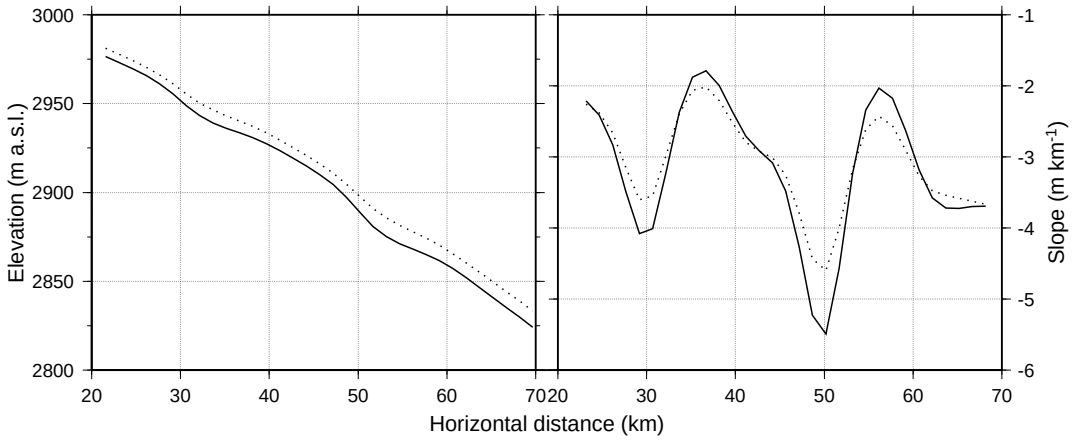

Figure 4: *Surface elevation (left panel) and surface gradients (right panel) for the steady-state experiment according to* HO *(solid line) and* SI *(dotted line).*

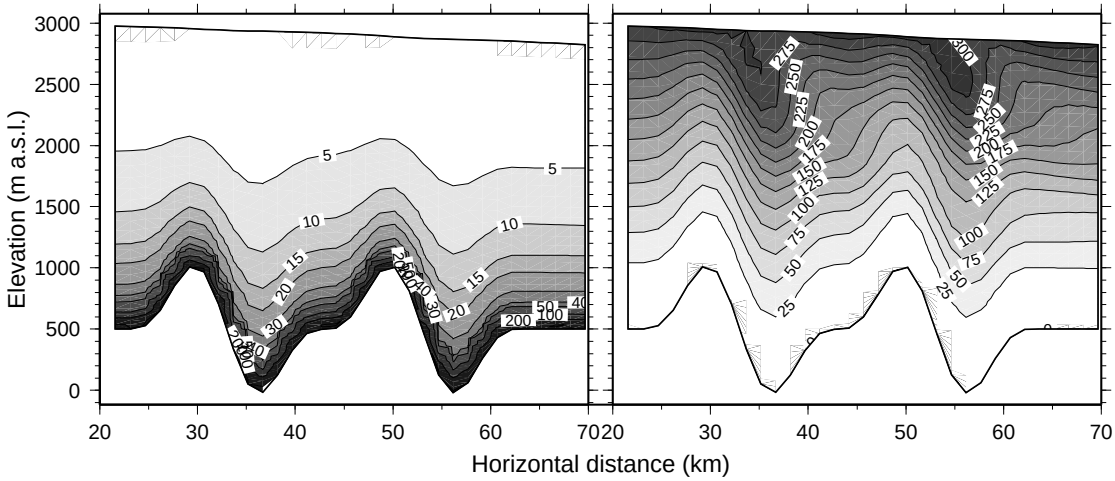

Figure 5: *Age determination in ka BP (left panel) and annual layer thickness in mm (right panel) for the steady-state experiment according to* HO. *Ice flow is from left to right.*

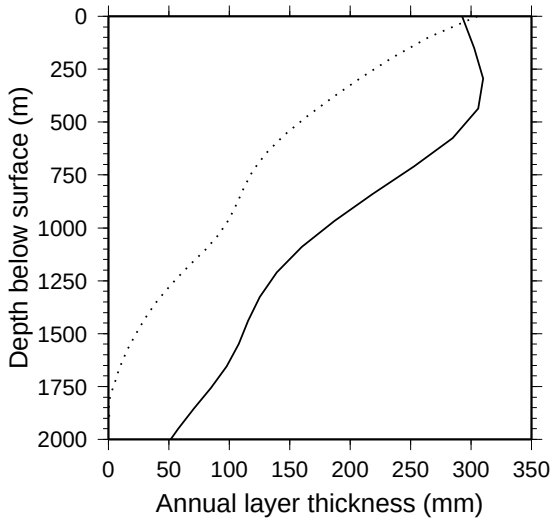

Figure 6: *Vertical profiles of annual layer thickness over a bump (dotted line) at x = 48 km, and over a trough (solid line) at x = 56 km. The surface mass balance is constant at both sites.*

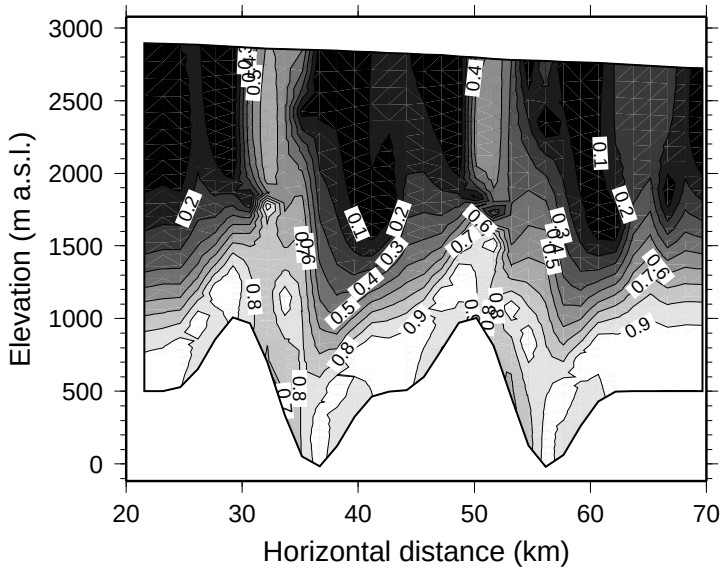

Figure 7: *Flank-flow index for the steady-state experiment according to* HO. *Low values (black) indicate pure shear, high values (white) indicate simple shear. Ice flow is from left to right.*